Statistics of temporal variations in the auroral electrojets over Fennoscandia

Simon Walker[1] (simon.walker@uib.no), Karl Laundal[1], Jone Reistad[1], Anders Ohma[1], Spencer Hatch[1]

[1]Birkeland Centre for Space Science, Department of Physics and Technology, University of Bergen, Norway

Key Points:

- A new inversion technique for Spherical Elementary Current analysis is implemented and tested
- A new data set enabling statistical and time dependent investigations of the auroral electrojets is produced
- We identify when and where temporal variations in the radial magnetic field are strongest

Corresponding author: Simon Walker, `simon.walker@uib.no`

Abstract

We present the implementation of an improved technique to coherently model the high-latitude ionospheric equivalent current. By using a favourable and fixed selection of 20 ground magnetometers in Fennoscandia, we present a method based on Spherical Elementary Current Systems (SECS) to model the currents coherently during 2000–2020. Due to the north-south extent of the ground stations used, we focus on the model output along the 105° magnetic meridian. In addition to the fixed data locations and SECS analysis grid, our improvements involve taking into account a priori knowledge of the large-scale current systems to improve the robustness of solving the underdetermined inverse problem. We account for contributions from ground induced currents assuming so-called mirror currents. An advantage of this data set over existing empirical models of ionospheric currents is the 1-min output resolution. High temporal resolution enables investigation of temporal changes in the magnetic field. We present an analysis of statistical properties of where (in magnetic latitude and local time) and at what rate ($\partial B_r/\partial t$) the radial magnetic field component fluctuates. We show that $\partial B_r/\partial t$, which is equivalent to the radial component of the curl of the induced electric field, is dependent on latitude, local time, and solar cycle. Other applications of the presented data set are also highlighted, including investigations of how Ultra Low Frequency oscillations in ground magnetic perturbations vary in space and time.

Plain Language Summary

The impact of the Sun's rays on the Earth's atmosphere generates the ionosphere, a part of the Earth's atmosphere where electrons and ions are able to flow separately. A number of Sun driven processes that can lead to phenomena such as the northern and southern lights, generate electric currents within the ionosphere. The magnetic field of these currents has been observed as early as the invention of the compass. In this study we use measurements of the magnetic field on the ground to estimate these currents and understand the processes that create them in greater detail. Beyond scientific curiosity, there is an importance to understanding this type of ionospheric dynamics. Variations in the magnetic field cause problems in applications such as oil drilling, which relies on magnetic field measurements for orientation, and power grids, which can be knocked out by large spikes in the current.

1 Introduction

The link between the Sun and geomagnetic field disturbances has been reported for a long time. In 1852 Sabine identified a link between the number of sunspots, which is an indicator of solar activity, and geomagnetic field disturbances. He found that during a minimum in the sunspot number we experience a reduction in geomagnetic field disturbances (W. Cliver & Cliver, 1994). Historical reports have shown that for centuries large scale features on the photosphere have coincided with observations of significant, intense geomagnetic activity in the form of low latitude aurora (Schove, 1983), however the mechanisms behind this were not understood. With the arrival of work by Chapman and Birkeland in the late 19th and early 20th century, the description of the Earth's magnetosphere submerged within the solar wind came into focus. Birkeland's early work introduced a current system, which bears his name, flowing in and out of the polar ionosphere. Despite his initial theories involving a stream of high velocity electrons being emitted from the Sun, he moved to the realisation of a neutral solar wind made up of both electrons and positively charged ions (Birkeland, 1908; Chapman & Ferraro, 1931). Although a different current system and theory outlined by Chapman prevailed for some time, with the arrival of space based magnetometers Birkeland's theory proved fruitful as it explained the magnetic field perturbations observed (Zmuda et al., 1966). Chapman and Ferraro's work transformed the field of space physics when they described how

magnetic storms are manifested through introduction of the magnetosphere and how it interacts with the solar wind (Chapman & Ferraro, 1931; Siscoe, 2001).

In more modern times we know that the solar wind is a quasi-neutral supersonic plasma streaming out of the Sun dragging with it the Sun's magnetic field, due to the frozen in effect, into interplanetary space. How this interplanetary magnetic field (IMF) couples with the Earth's magnetic field holds particular importance for the dynamics of the polar ionosphere and magnetosphere. This can be described by the Dungey cycle. The Dungey cycle is a generalised, simplified, steady state description of how, during periods of a southward oriented IMF, dayside geomagnetic flux is opened and reconnected with the IMF before being dragged over the polar cap, subsequently stimulating pre existing open flux in the magnetotail to reconnect. This newly closed flux then convects to the dayside magnetosphere (Dungey, 1961). In the region of the ionosphere, plasma flows are driven by the motion of magnetic flux around the ionosphere. At certain altitudes these plasma flows create a current system due to collisions between ions and neutrals causing a differential motion between the ions and electrons. Currents along the dawn and dusk flanks are referred to as the westward and eastward electrojets respectively. Ground magnetometers have been historically used to study the strength and extent of these electrojets. Such measurements are not affected by the magnetic field of the field aligned Birkeland currents and their associated connecting currents, a realisation made by Fukushima and thus has been named Fukushima's theorem. Fukushima's theorem states that under the approximation of a radial magnetic field (which is most valid in the polar regions), the magnetic signature of curl-free currents, whose source and sink are the Birkeland currents, cancel below the current layer (Fukushima, 1976). While, the magnetic signature of the divergence-free currents are observable above and below the current layer. Fukushima's theorem shows us why we needed space based magnetometers for Birkeland's theories to be confirmed (Zmuda et al., 1966; Fukushima, 1994). Harang utilised ground based magnetometers to identify a discontinuity between the westward and eastward electrojets (Harang, 1946; Koskinen & Pulkkinen, 1995). This discontinuity commonly coincides with the location of substorm onsets (Weygand et al., 2008). Consequently relating the electrojets to the closure of magnetotail flux described in the Dungey cycle.

There is an abundance of ground based magnetometers providing good coverage of measurements of the auroral electrojets. Particularly in regions such as North America and Fennoscandia. Spherical harmonic analysis has been a core part of modelling divergence-free ionospheric currents using ground based magnetometers. More recent techniques still have the methodology of Chapman and Bartels (1940) at their core (Laundal et al., 2016, 2018). However, the meaning of the spherical harmonic model output in regions where magnetometer coverage is sparse is often unclear and difficult to interpret. Amm (1997) introduced a technique called spherical elementary current systems which focuses on modelling limited regions. This approach models the divergence-free (DF) and curl-free (CF) components of the ionospheric currents on a 2D spherical shell independently using two different spherical elementary currents systems (SECS). Amm and Viljanen (1999) derived the magnetic field from the current a SECS produces. Therefore, we can recreate the magnetic field measured on ground using a weighted sum of DF SECS and consequently find a current that produces those magnetic field perturbations.

In previous studies DF SECS has proven to have a vast array of applications. Weygand et al. (2012) used DF SECS and ground magnetometers to produce estimates of the DF currents and compare them with measurements of convection with SuperDARN. During the summer they show that the DF currents can be used to predict the ionospheric convection, without the necessity of conditions for backscatter that limits the SuperDARN data set. In another study, the SECS amplitudes are compared with measurements of the region 1 and 2 currents using magnetometers on board the DMSP satellites (Weygand & Wing, 2016) and a significant resemblance is found. Many studies of the divergence-

free currents have focused on magnetospheric and ionospheric dynamics due to solar wind driving conditions and addressed questions of substorm onset phenomena (Weygand et al., 2011, 2021; Vanhamäki & Juusola, 2020). By placing SECS at both the ionospheric current layer and at a certain depth within the ground, the SECS method has been useful for separating observed magnetic perturbations into telluric and ionospheric sources (Pulkkinen, Amm, Viljanen, Korja, et al., 2003; Juusola et al., 2020).

In this study we build upon the DF SECS method and incorporate a new SECS inversion technique introduced by Laundal et al. (2021) for use with data from the Electrojet Zeeman Imaging Explorer (EZIE) mission, which will be launched in 2024. EZIE will be capable of making remote measurements of the magnetic field using the Zeeman effect (Yee et al., 2021). The inversion technique, used by Laundal et al. (2021), involves a priori information about the structure of the electrojet. Here we apply this technique to twenty ground magnetometers in Fennoscandia that were simultaneously available at 1-min resolution for a total of approximately 11 years between 2000 and 2020. The technique produces 2D maps of the electrojet and associated magnetic field, but we focus on an output along a 1D slice along the 105° magnetic meridian, in quasi-dipole co-ordinates, which is particularly well covered by the magnetometers. The resulting data set, which is publicly available (Walker et al., 2022b), consists of ground magnetic field perturbations and ionospheric sheet current densities along this meridian. We also highlight the interpretation of the time derivative of the radial magnetic field dB_r/dt as the radial component of the curl of the geomagnetically induced electric field (Vanhamäki et al., 2013) and present a statistical analysis of the properties of this quantity. This analysis stands in contrast to the analysis of the time derivative of the horizontal magnetic field (often denoted $\partial\mathbf{H}/\partial t$), which has received comparatively much more attention (Juusola et al., 2020; Tanskanen et al., 2001; Viljanen et al., 2001; Schillings et al., 2022; Weigel et al., 2003).

In Sections 2 and 3, we respectively present the data and our application of SECS to derive the divergence-free currents. In Section 4 we demonstrate the validity of the approach by comparing the large scale statistics of the divergence-free current and associated radial magnetic field structure with those of an empirical model (Laundal et al., 2018). We also present our statistical analysis of $\partial B_r/\partial t$. In Section 5 we discuss our findings, and in Section 6 we conclude the paper.

2 Data

We use data with 1-min time resolution from 20 magnetometers in Fennoscandia obtained through the SuperMAG collaboration (Gjerloev, 2012), see Figure 1. We use the version of the SuperMAG data which has the quiet-day Sq current contribution subtracted, along with the main field. SuperMAG also provides its data in local magnetic co-ordinates, in which the northward component points along the quiet-day horizontal component of the main magnetic field. Using the CHAOS-7 magnetic field model (Finlay et al., 2020) to obtain the declination angle at each station, the measured magnetic field vectors are rotated into the geodetic co-ordinate system.

To reduce ambiguity as to what causes variations in the modelled divergence-free currents, we require that all the magnetometers that are chosen for the SECS inversion are available at the same time. Figure 1 shows how often our twenty magnetometers are available individually and simultaneously (thick blue line). This combination of stations has been chosen to maximise the total coverage of simultaneous measurements, approximately 11 years over a period from 2000 to 2020. Figure 1 also shows the grid that we use in our analysis (discussed in Section 3), and the 105° magnetic meridian, where we evaluate the currents and magnetic field components. We see from the figure that this meridian passes through a high density of magnetometers.

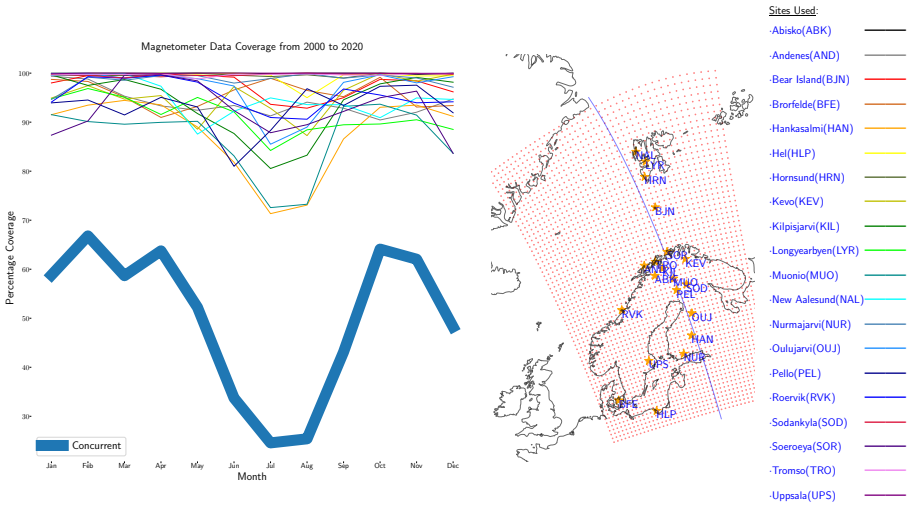

Figure 1. Left panel: Monthly data coverage of each chosen magnetometer and their availability concurrently. Right panel: SECS pole locations as red dots, orange stars to show the location of the magnetometers used in this study and a blue line that is the 105° magnetic meridian that the model is evaluated along

3 Method

In this study we apply a recently developed Spherical Elementary Current System (SECS) inversion technique to ground magnetometers. SECS analysis represents ionospheric and telluric currents as the weighted sum of multiple small-scale currents. The weights are determined from magnetometer measurements. It can thus be used as a way to interpolate magnetic fields and currents from a set of individual non-uniformly distributed magnetometers to a continuous map. Here we give a brief overview of the SECS analysis technique and describe our methodology.

Magnetic fields on ground can be modelled as 2D horizontal divergence-free currents that flow on spherical shells above and/ or below the Earth's surface (Chapman & Bartels, 1940). Such modelling has historically been accomplished using spherical harmonic analysis. Amm (1997) presented divergence-free basis functions that are more suitable for regional analyses, which he called Spherical Elementary Current Systems (SECS). The SECS basis functions are global but with a short reach. Placed sufficiently dense, and scaled appropriately, they can be used to represent any well-behaved 2D vector field on a sphere (Vanhamäki & Juusola, 2020). With these basis functions, a divergence-free surface current density $\vec{J}$ at a radius R can be written as

$$\vec{J}(\vec{r}) = \sum_i \frac{I_i \hat{\vec{e}}_{\phi_i}}{4\pi R} \cot(\frac{\theta_i}{2}) \tag{1}$$

where $\vec{r}$ is the position where $\vec{J}$ is evaluated. The sum is over a set of divergence-free SECS with amplitudes I_i. θ_i is the angular distance from the SECS to $\vec{r}$, and $\hat{\vec{e}}_{\phi_i}$ is an eastward unit vector in a coordinate system where the SECS is at the pole. In Equation 1 R could be above ground (above R_E, radius of the Earth), for modelling ionospheric currents, or below ground, for modelling telluric currents.

The magnetic field of one single divergence-free SECS was calculated by Amm and Viljanen (1999) through the Biot-Savart law. The analytic expressions for the θ (southward), ϕ (eastward), and r (radial) magnetic fields, in a local system centred on the SECS

pole, are:

$$\Delta B_{\theta_i}(\theta_i, r) = \frac{-\mu_0 I_i}{4\pi r \sin\theta_i} \begin{cases} \frac{s-\cos\theta_i}{\sqrt{1+s^2-2s\cos\theta_i}} + \cos\theta_i & r < R \\ \frac{1-s\cos\theta_i}{\sqrt{1+s^2-2s\cos\theta_i}} - 1 & r > R \end{cases} \tag{2}$$

$$\Delta B_{\phi_i}(\theta_i, r) = 0 \tag{3}$$

$$\Delta B_r(\theta_i, r) = \frac{\mu_0 I_i}{4\pi r} \begin{cases} \frac{1}{\sqrt{1+s^2-2s\cos\theta_i}} - 1 & r < R \\ \frac{s}{\sqrt{1+s^2-2s\cos\theta_i}} - s & r > R \end{cases} \tag{4}$$

$$s = \min(r, R)/\max(r, R). \tag{5}$$

In our case, we use magnetometers on ground, so $r = R_E$. However, we model currents both in the ionosphere ($R = R_I > R_E$) and below ground ($R = R_T < R_E$), so both versions of the equations are needed. These expressions are for a single elementary system, and the total magnetic field at $\vec{r}$ is the sum over all. This gives a linear relationship between magnetic field measurements and SECS amplitudes,

$$G\vec{m} = \vec{d}, \tag{6}$$

where $\vec{m}$ is a vector that contains the SECS amplitudes, $\vec{d}$ is a vector that contains all 60 magnetic field components from the 20 magnetometers, and G is a matrix that relates $\vec{m}$ and $\vec{d}$ according to the equations above. We return shortly to how we solve this system of equations for $\vec{m}$.

The grid of SECS can be as dense or as sparse as desired. Although a more dense grid of systems can capture finer structure, two points must be considered: (i) whether the measurements can resolve so fine a structure (for magnetometers one must take into account the spacing of the magnetometers and the smoothing of the magnetic signal with increasing distance from the source (Laundal et al., 2021)); (ii) a denser grid requires more model parameters, therefore solving for these parameters becomes more computationally expensive. We choose to place our elementary current systems above and below the ground in a grid that is regular in cubed sphere coordinates (Sadourny, 1972; Ronchi et al., 1996). The grid is displayed in the right panel in Figure 1, in a Lambert Conformal projection. The grid has been chosen with an average spacing of 50 km, positioned so that the magnetometers are not within 10 km of a SECS pole and oriented towards approximately magnetic north in magnetic Quasi-Dipole (QD) coordinates (Richmond, 1995), using an epoch of 2008. In total we have $N = 2814$ grid cells, with $2N$ elementary currents, one set above the ground at 110 km altitude, and one set below the ground.

We clearly have many more elementary current systems than data points, which means that the inverse problem of finding the SECS amplitudes from a small set of measurements is severely under-determined. This can be partly rectified by using a simplifying assumption about how the ionospheric currents are related to their induced counterpart in the ground. We choose that the radial magnetic field perturbations from the ionospheric and telluric currents exactly cancel at a 500 km depth (the telluric poles are placed at a depth derived from equation A5 in Juusola et al. (2016) that depends on the altitude of the ionospheric poles and the cancellation depth). Then, as detailed by Juusola et al. (2016), the mirror current magnitudes are precisely determined by the ionospheric current magnitudes, reducing the number of unknowns from $2N$ to N. This method ascribes the term "image currents" to the currents modelled by the telluric SECS poles. This name comes from the assumption that the telluric currents will mirror the ionospheric currents.

Even with this simplification, the problem remains under determined; there are an infinite number of SECS amplitude combinations that will fit the observations within some fixed precision. In this section we address the criteria in which we choose the solution to the inverse problem. Most recent studies that use SECS analysis (Pulkkinen, Amm, Viljanen, Korja, et al., 2003; Pulkkinen, Amm, & Viljanen, 2003; Amm, 1997; Wey-

gand et al., 2021; Vanhamäki & Juusola, 2020) handle this problem using truncated singular value decomposition (TSVD). By zeroing singular values below a certain cutoff, the spatial structure of the divergence-free current is encouraged to be smooth. In this paper we take an alternative approach, building on the recent study by Laundal et al. (2021), who presented a technique for SECS analysis for mesospheric magnetic field data from the upcoming EZIE satellite mission.

Following their approach, we find the set of SECS amplitudes, $\vec{m}$, that minimises

$$f = \|G\vec{m} - \vec{d}\|^2 + \lambda_1\|I\vec{m}\|^2 + \lambda_2\|L_e\vec{m}\|^2, \tag{7}$$

where I is the $N \times N$ identity matrix, and L_e is an $N \times N$ matrix that, when multiplied by $\vec{m}$, yields the gradient of the SECS amplitudes in the QD eastward direction. The first term in equation 7 is the sum of squared errors. If we only minimised this term, $\vec{m}$ would be the least squares solution. The second term represents the squared length of the model vector, multiplied by the parameter λ_1. Increasing λ_1 will limit the overall magnitude of the components in the solution vector, effectively decreasing the spatial complexity of the solution. Increasing λ_1 has a similar effect as increasing the cutoff value in a TSVD inversion. The third term in Equation 7 describes the sum of the squared magnitudes of the magnetic eastward gradients in the SECS amplitude, scaled by λ_2. Increasing λ_2 limits the eastward gradients. The rationale for including this term is that ionospheric electrodynamics tends to be structured east-west (Harang, 1946).

Since the location of our magnetometers and SECS poles are fixed, we choose a constant set of values for λ_1 and λ_2. If λ_1 is too much larger than λ_2 the amplitudes no longer have a smooth gradient in the magnetic east-west direction. If λ_2 is too much larger than λ_1 the amplitudes become thin bands in the east-west direction because there is no restriction in the variation in the north-south direction. Furthermore, even if the λ values are well balanced, if both are too large the model will not represent the data because the first term (the data-model misfit) will not be significant enough. With these things in mind, and after inspecting a great number of cases, we chose λ_1=10^{-23} and λ_2=10^{-21}. These numbers are based on the use of SI units. Since the magnetometer locations, SECS locations, and regularisation parameters are all fixed, our inversion results are directly comparable across the whole data set.

3.1 Examples

Figures 2 and 3 show two examples where the technique described above was applied. The left panels show the magnetic field on the ground, where the colour represents the radial magnetic field perturbations, and the arrows represent the horizontal component. The orange stars show the locations of the magnetometers. The red arrows represent the measured horizontal magnetic field and the coloured dot in the centre of the star the radial component. The second panels from the left shows the SECS pole amplitudes in colour. In the third panels, the arrows represent the modelled ionospheric currents and the colour its magnitude. The final panel shows a slice of the ionospheric currents along the 105° magnetic meridian, which is particularly well covered by data. The publicly available data set, Walker et al. (2022b), includes the ground magnetic field and equivalent current along this meridian, with spacing $\approx$ 70 km.

With equation 1, the divergence-free current can be calculated at, in principle, any location. However, very close to a SECS pole, the magnitude approaches infinity. Therefore, we follow Vanhamäki and Juusola (2020) and introduce a correction (see their Equation 2.44) closer than 50 km from the SECS poles. This correction is only applied when evaluating the divergence-free current, and not to the magnetic field, which is not as severely affected by the singularity due to the distance between the currents and the ground.

Figure 2 is based on 1 min of data taken at 22:34 UT on the 5th of February 2000. By looking at the left panel, we see that the model and the measurements are in good

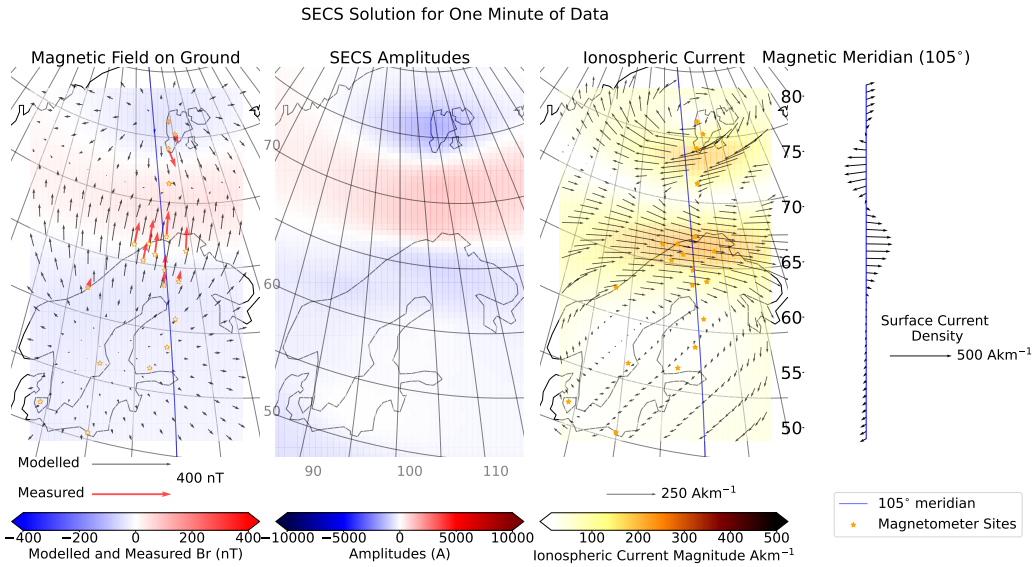

Figure 2. The left panel shows the estimated horizontal magnetic field as black quivers, the estimated radial magnetic field as the background colour, the location of the magnetometers as orange stars, the measured horizontal magnetic field as red quivers and measured radial magnetic as coloured dot in the centre of the stars. The second panel from the left shows the SECS pole amplitudes as the back ground colour. The third panel from the left shows the estimated divergence-free currents as black quivers and the magnitude of the currents with the background colour. The third panel from the left also shows the location of the magnetometers as orange stars. The right panel shows the estimated divergence-free currents along the 105° magnetic meridian, at different magnetic latitudes, as black quivers. The location and extent of the 105° magnetic meridian, where the model is evaluated for every minute of data, is shown as a blue line in the first panel and third panel from left. The time in UTC of the magnetometer data used for this inversion is 22:34 05/02/2000

agreement. The second panel clearly shows that the SECS amplitudes have small gradients in the east-west direction and shows large areas of similar amplitude. This is a clear case of a strong east-west electrojet. Figure 3 shows another example, based on one minute of magnetometer data at 20:25 UT on the same day. Again, the model and the measurements are in good agreement. Here, on the other hand, we see a strong northward current. This shows that the λ values in equation 7 are not so large as to prevent north-south structures when the data indicates that such structures exist.

4 Results

We now present results based on our data set, minute-cadence magnetic field perturbations and associated eastward and northward sheet current density along the 105° Quasi-Dipole meridian. First we compare the currents and radial magnetic field from an empirical model to a large-scale average based on our data set. This comparison is used as validation. The data set's relatively high time resolution enables investigation of spatiotemporal structures in a way that is not possible with empirical large-scale, average models. We therefore subsequently present an analysis of the temporal changes in the radial magnetic field ($\partial B_r/\partial t$).

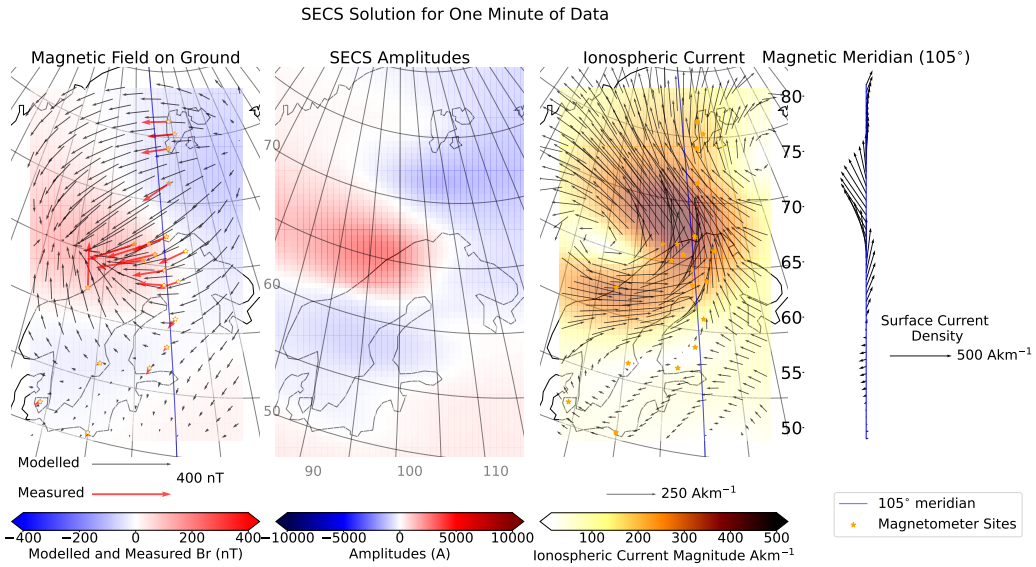

Figure 3. This figure uses the same set up as figure 2. The time in UTC of the magnetometer data used for this inversion is 20:25 05/02/2000

4.1 Large-scale average current structure

Here we compare a large-scale average current and radial magnetic field pattern to predictions from the Average Magnetic field and Polar current System (AMPS) model. The AMPS model (Laundal et al., 2018; Laundal & Toresen, 2018) is an empirical model of the ionospheric magnetic field and current system generated using magnetic field measurements from *Swarm* and the Challenging Minisatellite Payload (CHAMP) satellites. AMPS takes user inputs of solar F10.7cm flux, solar wind speed, IMF B_y and B_z, and the Earth's dipole tilt.

To compare our data set to AMPS predictions, we select our electrojet and radial magnetic field estimates when they occur during the following conditions: IMF B_y is between -5 nT and 5 nT, IMF B_z is between 0 nT and -10 nT, and the dipole tilt angle is less than 0°. Further measures are taken to ensure that the data selected is under the influence of these conditions by using a similar approach to Haaland et al. (2007): We apply a 30-minute rolling average to OMNI data (King & Papitashvili, 2005), that is time shifted to the bow shock, and associate it with our data set by having the average made up of OMNI data 20 minutes prior and 10 minutes after the SECS meridian was evaluated. Furthermore, we calculate the circular variance of IMF B_y and B_z in the same windows as a measure of how stable the conditions are. We then add a further selection criteria that the circular variance associated with our data set must be less than 0.04.

Figure 4 (left) shows the average horizontal sheet current and radial magnetic field based on this data selection, on a grid of magnetic latitude and local time. A corresponding AMPS prediction is shown on the right, using the mean conditions of the solar wind, IMF, solar flux and dipole tilt of the times selected to make the SECS based map. Figure 4 shows that the general shape of the radial magnetic field perturbations and electrojet are similar in the two approaches. This demonstrates that the technique produces results that are consistent with expectations from earlier studies. There are some notable differences between the two plots particularly in terms of the magnitude of the currents

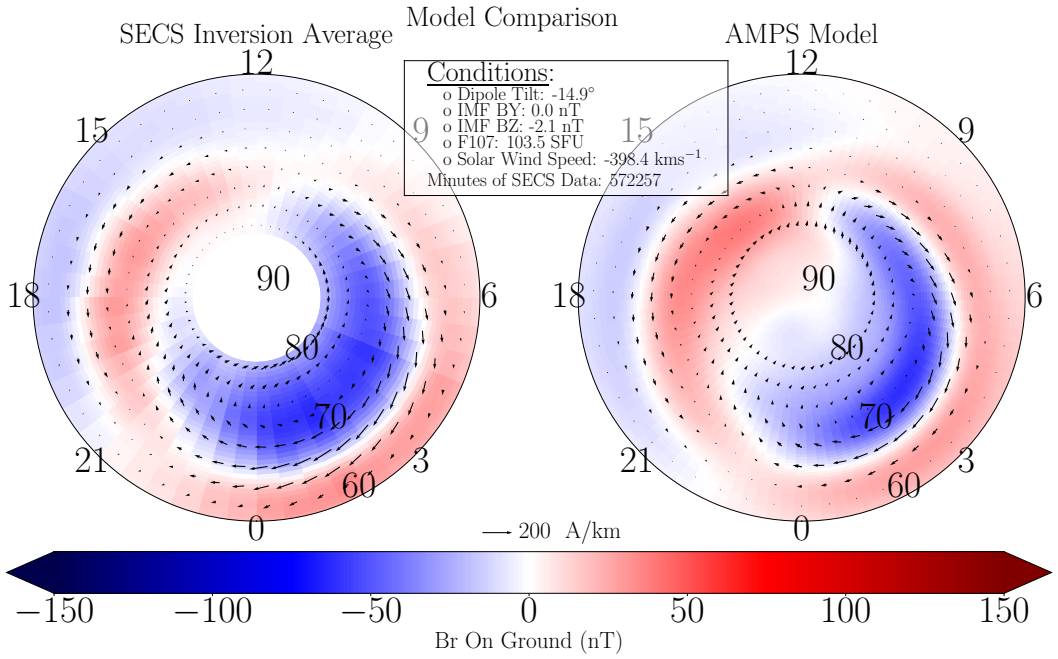

Figure 4. Left plot shows a polar view of the average divergence-free sheet current density and radial magnetic field perturbations on the ground for the SECS inversion. Right plot shows a polar view of the AMPS sheet current density and radial magnetic field perturbation under the conditions specified

and the radial magnetic field. We also see a difference in the shape and location of the cells of the radial magnetic field that are most prominent at higher latitudes. One difference between the two approaches is that the AMPS current by definition is divergence-free, while our average current pattern in general is not. Our technique enforces divergence-free currents at any given time, but averages composed of several meridians do not have this constraint. We reiterate that the main advantage of our approach over average models is that it allows analyses of spatio-temporal variations. We explore this further in the rest of this section.

4.2 Occurrence rate of large magnetic field variations

Temporal variations in the radial component of the magnetic field ($\partial B_r/\partial t$) are equivalent to the radial component of the curl of the purely induced (divergence-free) electric field, otherwise known as the geomagnetically induced electric field (GIE) (Vanhamäki et al., 2013). The large amount of data (11 years' worth of 1-min data, spanning 20 years), and the consistency in the technique makes our data set ideal for analysing how GIEs in Fennoscandia vary in relation to other parameters. This is also important for space weather applications, since variations in the magnetic field cause ground induced currents (GICs), which have negative consequences for human infrastructure, such as the electrical power grid (Oliveira & Ngwira, 2017; Molinski, 2002; Albertson et al., 1993).

Figure 5 shows the likelihood of observing temporal variations of the radial magnetic field perturbations (or equivalently, the radial component of the curl of GIEs) above a certain magnitude. The y axis shows the magnetic latitude, and the x axis shows the threshold for a positive detection. Negative x corresponds to decreases in B_r and positive x corresponds to increases. The colour and contours show the number of occurrences

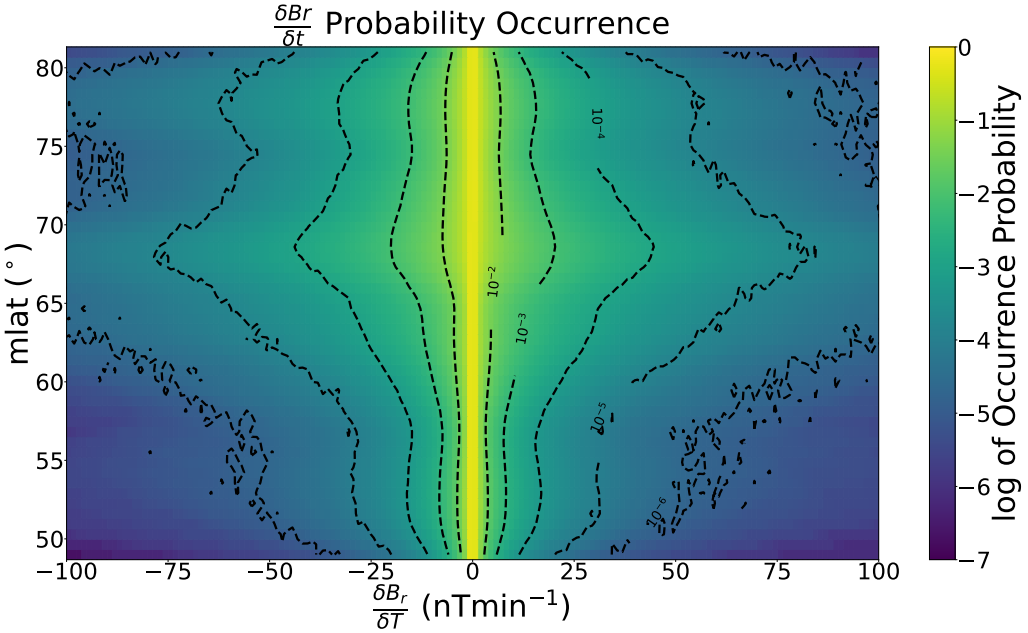

Figure 5. A plot of the statistics of fluctuations of the radial component of the magnetic field evaluated on the ground along the 105° meridian. The contours and colour are the cumulative probability of getting increases (decreases) in B_r that are at least the fluctuation indicated on the positive (negative) part of the x axis.

divided by the number of observations. The occurrence is presented in a logarithmic style where $10^{-5.7}$ is an occurrence of once per year. The figure is approximately symmetrical suggesting that large increases and large decreases are just as common at similar latitudes. Two peaks stand out, one that occurs at the northernmost coast of Norway and the second around the region of Svalbard, close to Ny-Ålesund. The larger of the two is near the average latitude of substorm disturbances and the location of the electrojets. The smaller of the two may be related to high latitude return currents. Explanations for the double peak are explored further in section 5.2.

Figure 6 shows the occurrence probability of large fluctuations as a function of magnetic local time and magnetic latitude. We choose to regard fluctuations greater than 25 nTmin^{-1} as large based on figure 5. We see two peaks, the largest again at latitudes close to the northern coast of Norway, and the second at latitudes near Ny–Ålesund. The strongest peak forms a smooth circle at similar latitudes for all MLTs, however exhibiting higher occurrence probability in the pre-midnight sector. This is the typical location for substorm onsets (Frey et al., 2004). The high latitude peak is strongest in the pre-midnight and pre-noon regions. The pre-midnight high-latitude peak may also be associated with substorms. We discuss the occurrence probability distribution in greater detail in section 5.2 and pay particular focus to the mechanisms that may be the cause of the pre-noon high latitude peak.

Figure 7 shows how the probability of large fluctuations in the radial magnetic field perturbation varies over the solar cycle. The occurrence probability is calculated by finding the meridians that have $\delta B_r/\delta t$ greater than 25 nT/min at any latitude. The occurrence probability shows an approximate 3 year offset with the peak in sunspot number and peaks during the declining phase. This is the same behaviour recorded in the solar wind velocity. This observation is in agreement with current literature where both

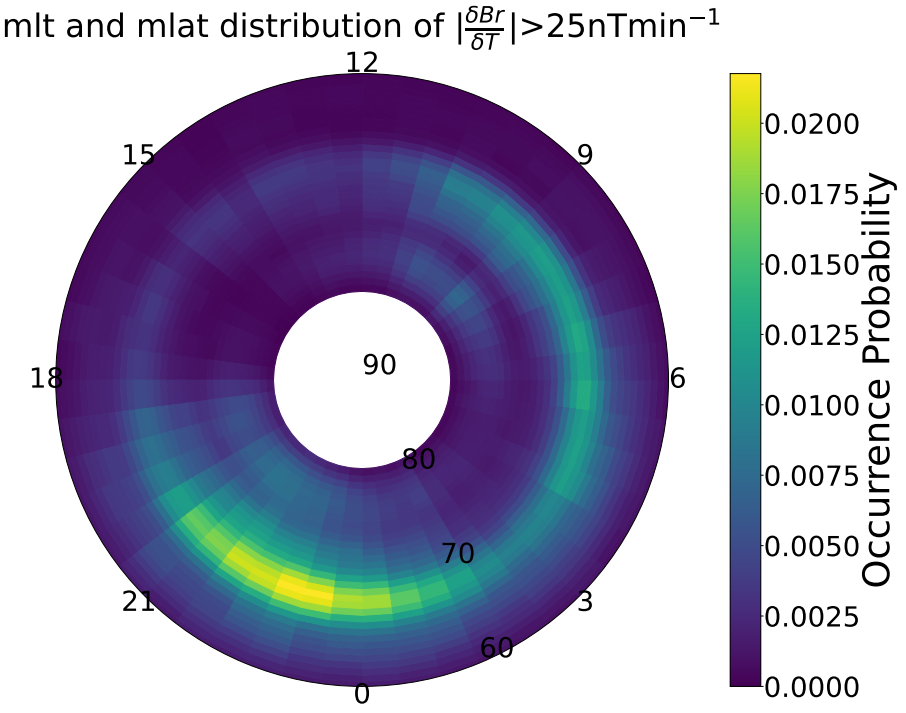

Figure 6. Figure showing the probability of a fluctuation of a radial magnetic field perturbation of magnitude greater than 25 nT/min. The figure is in mlt-mlat space where the colour represents the occurrence probability

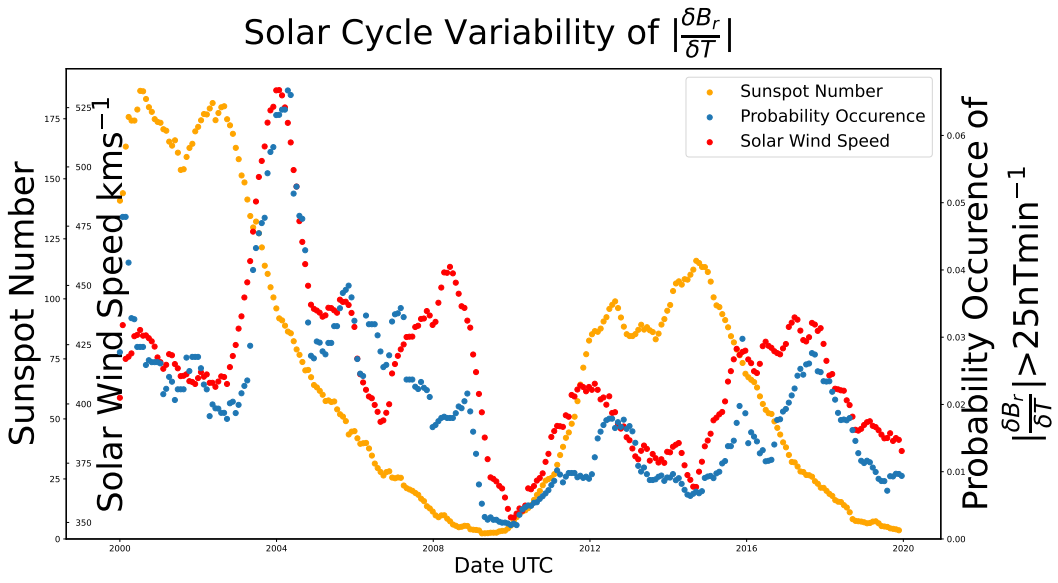

Figure 7. Figure showing the sunspot number, the solar wind speed, and the probability of observing fluctuations in B_r greater than 25 nT/min anywhere along the meridian. The quantities are first grouped into 27 days (one Carrington rotation), taking the mean, and then a 365 day window rolling mean is applied to remove relatively short time scale fluctuations.

wave phenomena and substorm occurrence statistics show a correlation with solar wind velocity (Tanskanen et al., 2005; Newell et al., 2016; Nosé et al., 1995; Nykyri et al., 2017; Hynönen et al., 2020; Dimmock et al., 2016).

5 Discussion

5.1 Relevance of the new dataset and technique

In this section we summarise the data set and the model introduced. We discuss the advantages of the approach used and the avenues of research where the dataset can contribute.

We have presented a technique to derive magnetic fields and equivalent currents along the 105° magnetic meridian, based on measurements from 20 magnetometers in Fennoscandia. Currents and magnetic field perturbations along this meridian are released in accompaniment with the paper (Walker et al., 2022b).

A comparable study is Aakjær et al. (2016) that utilises the magnetometers on board the European Space Agency's *Swarm* satellites. By using a similar approach to Olsen (1996), the auroral electrojet is modelled for each pass of a *Swarm* satellite by fitting a series of line currents orthogonal to the satellite track using the measured magnetic field magnitude. The use of satellites in Aakjær et al. (2016) has the advantage that they cover regions inaccessible to ground magnetometers. However, the *Swarm* satellites orbit above ≈450 km which means that their distance from the ionospheric current layer will limit the resolvable electrojet structure, compared to what can be achieved with a dense ground network. The constant location of measurements, the longevity of magnetometer operation and constant high latitude observations enables a much larger data set bringing greater confidence to the statistics produced and the ability to tackle temporal phenomena.

Compared to previous SECS based analyses of ground-based magnetometer measurements (Vanhamäki et al., 2003; Marsal et al., 2017; Weygand et al., 2011, 2012; Weygand & Wing, 2016), the present study is distinct in a number of ways: We keep a constant selection of ground magnetometers and SECS poles, thus keeping a constant model geometry, which allows us to produce a consistent data set that spans 20 years. This enables the study of long-term temporal variations and structures in the magnetic field, as demonstrated in section 4.1. We also use a regularisation scheme that is different from the truncated singular value decomposition, in order to encourage solutions that are aligned in the magnetic east-west direction unless the data indicates otherwise.

In this study we use the regularisation approach introduced by Laundal et al. (2021) for the application to the Electrojet Zeeman Imaging Explorer(EZIE) satellites that are planned for launch in 2024. EZIE will remotely detect the magnetic field at ≈80 km altitude using the Zeeman effect (Yee et al., 2021). At this altitude the influence of telluric currents is negligible. The high density of measurements and their vicinity to the electrojet will allow EZIE to resolve fine structures in the electrojets. One application of EZIE, as a continuation of this and other studies, is to utilise two layers of measurements (EZIE and ground magnetometers) to improve the separation of magnetic fields from telluric and ionospheric currents. Combining EZIE measurements at 80 km altitude with both ground and low Earth orbit measurements of magnetic perturbations will allow for further investigation of large and small scale features with unprecedented 3D coverage.

There are many avenues to developing this technique further. Firstly, the methodology by Juusola et al. (2020) can be used to improve upon the approach used to account for the influence of telluric currents, thus modelling the ionospheric currents more accurately. Secondly, much like Green et al. (2007) did with spherical cap harmonics, we

can use a combination of ground and satellite measurements of the magnetic field to constrain a superposition of DF and CF SECS (Amm, 1997; Amm & Viljanen, 1999). This allows us to take advantage of a regional approach to estimate currents with finer structure than is achieved by the Active Magnetosphere and Planetary Response Experiment (AMPERE) (Anderson et al., 2014). Furthermore, we can now use shorter data windows than Green et al. (2007). We can then analyse the ionospheric currents at time scales closer to substorm dynamics. Unlike other studies (Laundal et al., 2022) we will estimate the ionospheric currents based only on the magnetic field data, without further knowledge of the ionospheric state.

5.2 $\partial B_r/\partial t$

Figures 5 and 6 show that there are two clear peaks in the probability of large temporal variations in B_r, one at auroral latitudes and one at higher latitudes. There are several possible explanations for the latitudinal distribution of the occurrence of large fluctuations in the radial magnetic field: The density of magnetometers is necessarily smaller in the ocean region between northern Norway and Svalbard, with a single magnetometer at Bjørnøya. This may increase the relative importance of the damping terms in our cost function (Equation 7), leading to a smaller B_r and thus smaller $\partial B_r/\partial t$. Another explanation is that the peak coincides with the peak in the latitudinal distribution of electrojets.

An alternative geological explanation for the double peak is that the difference between the high conducting sea water and less conductive ground around coastal magnetometers leads to an enhanced radial magnetic field from the induced currents, as discussed by Juusola et al. (2020). The method that we use to take into account ground-induced currents is incapable of accounting for this effect of varying conductivity. While this does not affect our estimates of the magnetic field it will affect our estimates of the divergence-free ionospheric current. A repeat of this study on magnetometers in other regions may allow us to eliminate the effects of geography in the model by comparing the occurrence distributions from the different data sets. Improved techniques in accounting for the influence of telluric currents, such as that presented by Juusola et al. (2020), can be used in future research to perform a better separation of the ionospheric and telluric contributions to the magnetometer measurements. In any case, improving our model of the telluric currents is not likely to have any influence on the results shown in Figures 5–7 as we are fitting B_r, and either approach will be a similar interpolation of the measurements of the radial magnetic field perturbation.

The MLT distribution, as shown in figure 6, is not hampered by such geological effects. Therefore the MLT distribution and latitudinal distribution, excluding the region between the Norwegian coast and Svalbard, can be interpreted in terms of ionospheric dynamics. Figure 6 shows that there is a peak in the occurrence of large $\partial B_r/\partial t$ at the common location of substorm onsets, 23 h MLT, with a second peak at high latitudes at around 9 h MLT. We also observe but have not presented that the time derivative of the horizontal magnetic field, as reported by Viljanen et al. (2001), evinces a similar MLT and MLAT distribution. In figure 6 we also see a peak in the occurrence probability at high latitudes in the pre-noon sector. This peak may be associated with the current driven by a rapid solar wind pressure increase as described by Madelaire et al. (2022). This hypothesis can be addressed in future work by reproducing these statistics under common favourable conditions, such as a northward orientated IMF, to see if the features in the statistics become enhanced. Another theory is that the peak is related to a high occurrence of ULF waves. Conditions are known to be favourable for ULF waves in the solar wind on the dawn side of the magnetosphere (Plaschke et al., 2018). Nosé et al. (1995) identified a distribution in ULF waves, from the magnetometer on-board Dynamics Explorer 1, that also peaks pre-noon at a high latitude. Furthermore, Weigel et al. (2003) investigated the time derivative of the horizontal magnetic field and found the occurrence

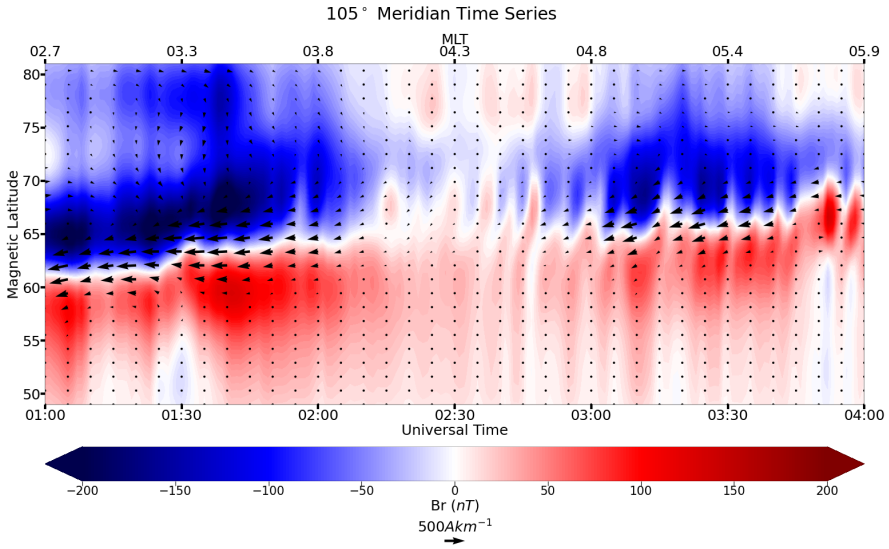

Figure 8. Time series of the data set with sheet current density vectors reduced to a cadence of 5 minutes and 25 data points along the meridian. The data is from the morning sector on the 28th of January 2000

of strong $\delta H/\delta t$ at a similar location, attributing this peak to the influence of ULF waves. Section 5.3 shows that the SECS methodology implemented in this study does reproduce waves and can be used to investigate such phenomena. The hypothesis, in regards to the distribution of ULF waves, can be addressed in future work by analysing the periodicity of these fluctuations and their contribution to the presented statistics.

5.3 ULF wave visualization

Figure 8 shows an example of the magnetic field and divergence-free current at the 105° meridian as a function of time and MLT. The colour shows the radial magnetic field on ground, including both ionospheric and internal contributions. The vectors show the equivalent current corresponding to the ionospheric contribution to the observed magnetic field. The figure was produced by stacking vertical latitudinal profiles horizontally. The lower x-axis shows the universal time, and the top x-axis shows the magnetic local time of the 105° meridian. This "magnetic field keogram" shows how the electrojet can change over time and how the zero point of the radial magnetic field perturbations tracks the centre of the electrojet.

Figure 8 shows clear evidence of ULF waves in periodic fluctuations of the radial magnetic field perturbations. This is most clearly seen between 2:10 and 3:00 universal time (UT). The figure illustrates that the 1-min resolution magnetic field model, evaluated along the 105° meridian allows easy visual identification of waves, and wave characteristics such as amplitude, phase and frequency. An investigation into the occurrence and magnitude of ULF waves could help test the hypothesis presented in section 4.2, that the pre-noon high latitude peak may be explained by such phenomena.

5.4 Future Studies

The technique presented here is also applicable with other datasets. A number of magnetometers have higher cadence measurements than are used in this study. The IM-

AGE chain has a 10-s cadence for all their magnetometers, some even have 1-s cadence. Using these magnetometers, this study could be repeated and higher frequency waves in the magnetic field evaluated along the meridian could be resolved. Lastly, as stated previously, the methodology could be applied to different regions and the study repeated. For example, North America has great coverage on magnetometers; performing a similar study using those magnetometers could allow us to verify or refute the geological hypotheses surrounding the peaks in the latitudinal distribution of the occurrence of large $\partial B_r/\partial t$. The study can also be repeated for conjugate chains of magnetometers, such as those in Greenland and Antarctica, to investigate inter-hemispheric differences.

6 Conclusions

We have presented a new technique for the application of divergence-free Spherical Elementary Current Systems (SECS) and applied it to twenty ground magnetometers in Fennoscandia. This has yielded a new data set of divergence-free currents along the 105° magnetic meridian covering the period of 2000 to 2020, with the total amount of data being 11 years at one-minute cadence. The dataset is publicly available (Walker et al., 2022b). It has been demonstrated that large scale average patterns of this data set follow expected behaviour. Furthermore, we have used this data set to investigate the temporal and spatial variations in the auroral electrojets and the radial magnetic field. Particularly the radial magnetic field from this data set clearly evinces the presence of wave phenomena. We have also presented statistics of the fluctuations of the radial magnetic field and we find that there are clear peak locations, in magnetic local time and magnetic latitude.

7 Data Availability Statement

The code for producing Figures 4–6 and figure 8 is available at Walker et al. (2022a). The ground magnetometer data has been retrieved from the SuperMAG collaboration: `https://supermag.jhuapl.edu/mag`, where data from all stations can be downloaded as yearly files. The solar wind and interplanetary magnetic field measurements has been downloaded from the OMNI database: `https://cdaweb.gsfc.nasa.gov/sp_phys/data/omni/hro_1min/`. The sunspot number has been retrieved from SILSO: `https://www.sidc.be/silso/datafiles`

Acknowledgments

This work was supported by Research Council of Norway under contracts 223252/F50 and 300844/ F50 and by the Trond Mohn Foundation. For the ground magnetometer data we thank the institutes who maintain the IMAGE Magnetometer Array: Tromsø Geophysical Observatory of UiT the Arctic University of Norway (Norway), Finnish Meteorological Institute (Finland), Institute of Geophysics Polish Academy of Sciences (Poland), GFZ German Research Centre for Geosciences (Germany), Geological Survey of Sweden (Sweden), Swedish Institute of Space Physics (Sweden), Sodankylä Geophysical Observatory of the University of Oulu (Finland), Polar Geophysical Institute (Russia), and DTU Technical University of Denmark (Denmark). For the processing, baseline removal and distribution of the ground magnetometer data we acknowledge: SuperMAG, PI Jesper W. Gjerloev. For the sunspot number we acknowledge: The World Data Center SILSO, Royal Observatory of Belgium, Brussels. We extend our gratitude to the members of the Understanding Mesoscale Ionospheric Electrodynamics Using Regional Data Assimilation team for the discussions and insight into the topic of study. We also thank the International Space Science Institute in Bern, Switzerland for hosting the team.

References

Aakjær, C. D., Olsen, N., & Finlay, C. C. (2016, 8). Determining polar ionospheric electrojet currents from Swarm satellite constellation magnetic data. *Earth, Planets and Space*, *68*(1), 1–14. Retrieved from https://earth-planets-space.springeropen.com/articles/10.1186/s40623-016-0509-y doi: 10.1186/s40623-016-0509-y

Albertson, V. D., Bozoki, B., Feero, W. E., Kappenman, J. G., Larsen, E. V., Nordell, D. E., ... Walling, R. (1993). Geomagnetic disturbance effects on power systems. *IEEE Transactions on Power Delivery*, *8*(3), 1206–1216. doi: 10.1109/61.252646

Amm, O. (1997, 7). *Ionospheric Elementary Current Systems in Spherical Coordinates and Their Application* (Vol. 49; Tech. Rep. No. 7). Retrieved from http://joi.jlc.jst.go.jp/JST.Journalarchive/jgg1949/49.947?from=CrossRef doi: 10.5636/jgg.49.947

Amm, O., & Viljanen, A. (1999). Ionospheric disturbance magnetic field continuation from the ground to the ionosphere using spherical elementary current systems. *Earth, Planets and Space*, *51*(6), 431–440. doi: 10.1186/BF03352247

Anderson, B. J., Korth, H., Waters, C. L., Green, D. L., Merkin, V. G., Barnes, R. J., & Dyrud, L. P. (2014, 5). Development of large-scale Birkeland currents determined from the Active Magnetosphere and Planetary Electrodynamics Response Experiment. *Geophysical Research Letters*, *41*(9), 3017–3025. Retrieved from http://doi.wiley.com/10.1002/2014GL059941 doi: 10.1002/2014GL059941

Birkeland, K. (1908). *The Norwegian aurora polaris expedition, 1902-1903.* Christiania,: H. Aschelhoug,. Retrieved from https://www.biodiversitylibrary.org/bibliography/17857 doi: 10.5962/bhl.title.17857

Chapman, S., & Bartels, J. (1940). Geomagnetism, Vol. II: Analysis of the Data, and Physical Theories. *Geomagnetism*.

Chapman, S., & Ferraro, V. C. A. (1931). A new theory of magnetic storms. *Terrestrial Magnetism and Atmospheric Electricity*, *36*(2), 77–97. Retrieved from https://onlinelibrary.wiley.com/doi/abs/10.1029/TE036i002p00077 doi: 10.1029/TE036i002p00077

Dimmock, A. P., Nykyri, K., Osmane, A., & Pulkkinen, T. I. (2016, 7). Statistical mapping of ULF Pc3 velocity fluctuations in the Earth's dayside magnetosheath as a function of solar wind conditions. *Advances in Space Research*, *58*(2), 196–207. doi: 10.1016/j.asr.2015.09.039

Dungey, J. W. (1961, 1). Interplanetary magnetic field and the auroral zones. *Physical Review Letters*, *6*(2), 47–48. Retrieved from https://journals.aps.org/prl/abstract/10.1103/PhysRevLett.6.47 doi: 10.1103/PhysRevLett.6.47

Finlay, C. C., Kloss, C., Olsen, N., Hammer, M. D., Tøffner-Clausen, L., Grayver, A., & Kuvshinov, A. (2020, 12). The CHAOS-7 geomagnetic field model and observed changes in the South Atlantic Anomaly. *Earth, Planets and Space*, *72*(1), 1–31. Retrieved from https://doi.org/10.1186/s40623-020-01252-9 doi: 10.1186/s40623-020-01252-9

Frey, H. U., Mende, S. B., Angelopoulos, V., & Donovan, E. F. (2004, 10). Substorm onset observations by IMAGE-FUV. *Journal of Geophysical Research: Space Physics*, *109*(A10). Retrieved from https://agupubs.onlinelibrary.wiley.com/doi/full/10.1029/2004JA010607 doi: 10.1029/2004JA010607

Fukushima, N. (1976). Generalized theorem for no ground magnetic effect of vertical currents connected with Pedersen currents in the uniform-conductivity ionosphere. *Report of Ionosphere and Space Research in Japan*, *30*(1-2), 35–40.

Fukushima, N. (1994, 10). Some topics and historical episodes in geomagnetism and aeronomy. *Journal of Geophysical Research*, *99*(A10), 19113. Retrieved from https://agupubs.onlinelibrary.wiley.com/doi/full/10.1029/94JA00102 doi: 10.1029/94ja00102

Gjerloev, J. W. (2012). The SuperMAG data processing technique. *Journal of Geophysical Research: Space Physics*, *117*(9). doi: 10.1029/2012JA017683

Green, D. L., Waters, C. L., Korth, H., Anderson, B. J., Ridley, A. J., & Barnes, R. J. (2007, 5). Technique: Large-scale ionospheric conductance estimated from combined satellite and ground-based electromagnetic data. *Journal of Geophysical Research: Space Physics*, *112*(5), n/a-n/a. Retrieved from http://doi.wiley.com/10.1029/2006JA012069 doi: 10.1029/2006JA012069

Haaland, S. E., Paschmann, G., Förster, M., Quinn, J. M., Torbert, R. B., McIlwain, C. E., ... Kletzing, C. A. (2007). High-latitude plasma convection from Cluster EDI measurements: Method and IMF-dependence. *Annales Geophysicae*, *25*(1), 239–253. doi: 10.5194/angeo-25-239-2007

Harang, L. (1946). The mean field of disturbance of polar geomagnetic storms. *Journal of Geophysical Research*, *51*(3), 353. doi: 10.1029/te051i003p00353

Hynönen, R., Tanskanen, E. I., & Francia, P. (2020). Solar cycle evolution of ULF wave power in solar wind and on ground. *Journal of Space Weather and Space Climate*, *10*, 43. Retrieved from https://www.swsc-journal.org/articles/swsc/full_html/2020/01/swsc190018/swsc190018.html doi: 10.1051/swsc/2020046

Juusola, L., Kauristie, K., Vanhamäki, H., Aikio, A., & van de Kamp, M. (2016, 9). Comparison of auroral ionospheric and field-aligned currents derived from Swarm and ground magnetic field measurements. *Journal of Geophysical Research A: Space Physics*, *121*(9), 9256–9283. Retrieved from https://onlinelibrary.wiley.com/doi/abs/10.1002/2016JA022961 doi: 10.1002/2016JA022961

Juusola, L., Vanhamäki, H., Viljanen, A., & Smirnov, M. (2020, 9). Induced currents due to 3D ground conductivity play a major role in the interpretation of geomagnetic variations. *Annales Geophysicae*, *38*(5), 983–998. doi: 10.5194/angeo-38-983-2020

King, J. H., & Papitashvili, N. E. (2005). Solar wind spatial scales in and comparisons of hourly Wind and ACE plasma and magnetic field data. *Journal of Geophysical Research: Space Physics*, *110*(A2), A02104. doi: 10.1029/2004JA010649

Koskinen, H. E. J., & Pulkkinen, T. I. (1995). Midnight velocity shear zone and the concept of Harang discontinuity. *Journal of Geophysical Research*, *100*(A6), 9539. doi: 10.1029/95ja00228

Laundal, K. M., Finlay, C. C., Olsen, N., & Reistad, J. P. (2018, 5). Solar Wind and Seasonal Influence on Ionospheric Currents From Swarm and CHAMP Measurements. *Journal of Geophysical Research: Space Physics*, *123*(5), 4402–4429. Retrieved from https://onlinelibrary.wiley.com/doi/full/10.1029/2018JA025387 doi: 10.1029/2018JA025387

Laundal, K. M., Gjerloev, J. W., Østgaard, N., Reistad, J. P., Haaland, S., Snekvik, K., ... Milan, S. E. (2016, 3). The impact of sunlight on high-latitude equivalent currents. *Journal of Geophysical Research A: Space Physics*, *121*(3), 2715–2726. Retrieved from https://onlinelibrary.wiley.com/doi/10.1002/2015JA022236 doi: 10.1002/2015JA022236

Laundal, K. M., Reistad, J. P., Hatch, S. M., Madelaire, M., Walker, S. J., Hovland, A. Ø., ... Sorathia, K. A. (2022, 5). Local Mapping of Polar Ionospheric Electrodynamics. *Journal of Geophysical Research: Space Physics*, *127*(5). Retrieved from https://onlinelibrary.wiley.com/doi/10.1029/2022JA030356 doi: 10.1029/2022JA030356

Laundal, K. M., & Toresen, M. (2018). *klaundal/pyAMPS: pyAMPS 0.1.0.* Retrieved from https://zenodo.org/record/1182931 doi: 10.5281/ZENODO.1182931

Laundal, K. M., Yee, J.-H. H., Merkin, V. G., Gjerloev, J. W., Vanhamäki, H., Reis-

tad, J. P., ... Espy, P. J. (2021, 5). Electrojet estimates from mesospheric magnetic field measurements. *Journal of Geophysical Research: Space Physics*, *126*(5), 1–17. Retrieved from https://onlinelibrary.wiley.com/doi/full/10.1029/2020JA028644 doi: 10.1029/2020ja028644

Madelaire, M., Laundal, K. M., Reistad, J. P., Hatch, S. M., & Ohma, A. (2022, 8). Transient high latitude geomagnetic response to rapid increases in solar wind dynamic pressure. *Frontiers in Astronomy and Space Sciences*, *9*, 188. doi: 10.3389/FSPAS.2022.953954/BIBTEX

Marsal, S., Torta, J. M., Segarra, A., & Araki, T. (2017, 1). Use of spherical elementary currents to map the polar current systems associated with the geomagnetic sudden commencements on 2013 and 2015 St. Patrick's Day storms. *Journal of Geophysical Research: Space Physics*, *122*(1), 194–211. Retrieved from https://onlinelibrary.wiley.com/doi/abs/10.1002/2016JA023166 doi: 10.1002/2016JA023166

Molinski, T. S. (2002, 11). Why utilities respect geomagnetically induced currents. *Journal of Atmospheric and Solar-Terrestrial Physics*, *64*(16), 1765–1778. doi: 10.1016/S1364-6826(02)00126-8

Newell, P. T., Liou, K., Gjerloev, J. W., Sotirelis, T., Wing, S., & Mitchell, E. J. (2016, 8). Substorm probabilities are best predicted from solar wind speed. *Journal of Atmospheric and Solar-Terrestrial Physics*, *146*, 28–37. doi: 10.1016/j.jastp.2016.04.019

Nosé, M., Iyemori, T., Sugiura, M., & Slavin, J. A. (1995, 8). A strong dawn/dusk asymmetry in Pc5 pulsation occurrence observed by the DE-1 satellite. *Geophysical Research Letters*, *22*(15), 2053–2056. Retrieved from https://onlinelibrary.wiley.com/doi/full/10.1029/95GL01794 doi: 10.1029/95GL01794

Nykyri, K., Ma, X., Dimmock, A., Foullon, C., Otto, A., & Osmane, A. (2017, 9). Influence of velocity fluctuations on the Kelvin-Helmholtz instability and its associated mass transport. *Journal of Geophysical Research: Space Physics*, *122*(9), 9489–9512. Retrieved from https://onlinelibrary.wiley.com/doi/full/10.1002/2017JA024374 doi: 10.1002/2017JA024374

Oliveira, D. M., & Ngwira, C. M. (2017). Geomagnetically Induced Currents: Principles. *Brazilian Journal of Physics*, *47*(5), 552–560. Retrieved from http://wdc.kugi.kyoto-u.ac.jp/index.html doi: 10.1007/s13538-017-0523-y

Olsen, N. (1996, 12). A new tool for determining ionospheric currents from magnetic satellite data. *Geophysical Research Letters*, *23*(24), 3635–3638. Retrieved from https://onlinelibrary.wiley.com/doi/full/10.1029/96GL02896 doi: 10.1029/96GL02896

Plaschke, F., Hietala, H., Archer, M., Blanco-Cano, X., Kajdič, P., Karlsson, T., ... Sibeck, D. (2018, 8). *Jets Downstream of Collisionless Shocks* (Vol. 214) (No. 5). Springer Netherlands. Retrieved from https://link.springer.com/article/10.1007/s11214-018-0516-3 doi: 10.1007/s11214-018-0516-3

Pulkkinen, A., Amm, O., & Viljanen, A. (2003). Separation of the geomagnetic variation field on the ground into external and internal parts using the spherical elementary current system method. *Earth, Planets and Space*, *55*(3), 117–129. doi: 10.1186/BF03351739

Pulkkinen, A., Amm, O., Viljanen, A., Korja, T., Hjelt, S. E., Kaikkonen, P., ... Tregubenko, V. (2003, 2). Ionospheric equivalent current distributions determined with the method of spherical elementary current systems. *Journal of Geophysical Research: Space Physics*, *108*(A2). Retrieved from http://doi.wiley.com/10.1029/2001JA005085 doi: 10.1029/2001JA005085

Richmond, A. (1995, 1). Ionospheric Electrodynamics. In Hans Volland (Ed.), *Handbook of atmospheric electrodynamics* (Vol. 1, pp. 249–290). CRC Press. doi: 10.1201/9780203713297

Ronchi, C., Iacono, R., & Paolucci, P. S. (1996, 3). The ".Cubed sphere":

A new method for the solution of partial differential equations in spherical geometry. *Journal of Computational Physics*, *124*(1), 93–114. doi: 10.1006/jcph.1996.0047

Sadourny, R. (1972). Conservative Finite-Difference Approximations of the Primitive Equations on Quasi-Uniform Spherical Grids. *Monthly Weather Review*, *100*(2), 136–144. Retrieved from https://journals.ametsoc.org/view/journals/mwre/100/2/1520-0493_1972_100_0136_cfaotp_2_3_co_2.xml doi: 10.1175/1520-0493(1972)100⟨0136:CFAOTP⟩2.3.CO;2

Schillings, A., Palin, L., Opgenoorth, H. J., Hamrin, M., Rosenqvist, L., Gjerloev, J. W., ... Barnes, R. (2022, 5). Distribution and Occurrence Frequency of dB/dt Spikes During Magnetic Storms 1980–2020. *Space Weather*, *20*(5). doi: 10.1029/2021SW002953

Schove, D. J. (1983). *Sunspot cycles.*

Siscoe, G. L. (2001). 70 years of magnetospheric modeling. In *Geophysical monograph series* (Vol. 125, pp. 211–227). American Geophysical Union (AGU). Retrieved from https://onlinelibrary.wiley.com/doi/full/10.1029/GM125p0211 doi: 10.1029/GM125p0211

Tanskanen, E. I., Slavin, J. A., Tanskanen, A. J., Viljanen, A., Pulkkinen, T. I., Koskinen, H. E., ... Eastwood, J. (2005, 8). Magnetospheric substorms are strongly modulated by interplanetary high-speed streams. *Geophysical Research Letters*, *32*(16), 1–4. Retrieved from https://onlinelibrary.wiley.com/doi/full/10.1029/2005GL023318 doi: 10.1029/2005GL023318

Tanskanen, E. I., Viljanen, A., Pulkkinen, T. I., Pirjola, R., Häkkinen, L., Pulkkinen, A., & Amm, O. (2001, 7). At substorm onset, 40% of AL comes from underground. *Journal of Geophysical Research: Space Physics*, *106*(A7), 13119–13134. doi: 10.1029/2000ja900135

Vanhamäki, H., Amm, O., & Viljanen, A. (2003, 6). One-dimensional upward continuation of the ground magnetic field disturbance using spherical elementary current systems. *Earth, Planets and Space*, *55*(10), 613–625. Retrieved from https://earth-planets-space.springeropen.com/articles/10.1186/BF03352468 doi: 10.1186/BF03352468

Vanhamäki, H., & Juusola, L. (2020). Introduction to Spherical Elementary Current Systems. In *Ionospheric multi-spacecraft analysis tools* (pp. 5–33). Springer International Publishing. doi: 10.1007/978-3-030-26732-2{_}2

Vanhamäki, H., Viljanen, A., Pirjola, R., & Amm, O. (2013, 10). Deriving the geomagnetically induced electric field at the Earth's surface from the time derivative of the vertical magnetic field. *Earth, Planets and Space*, *65*(9), 997–1006. Retrieved from https://earth-planets-space.springeropen.com/articles/10.5047/eps.2013.03.013 doi: 10.5047/eps.2013.03.013

Viljanen, A., Nevanlinna, H., Pajunpää, K., & Pulkkinen, A. (2001). Time derivative of the horizontal geomagnetic field as an activity indicator. *Annales Geophysicae*, *19*(9), 1107–1118. doi: 10.5194/angeo-19-1107-2001

Walker, S. J., Laundal, K. M., Reistad, J. P., Hatch, S. M., & Ohma, A. (2022a). *08walkersj/SECpy_Plotting: SECpy_Plotting 0.1.0.* Retrieved from https://zenodo.org/record/7138948#.Yz0_uNJByEA doi: 10.5281/zenodo.7138948

Walker, S. J., Laundal, K. M., Reistad, J. P., Hatch, S. M., & Ohma, A. (2022b). *Statistics of temporal variations in the auroral electrojets over Fennoscandia- Dataset.* Retrieved from https://zenodo.org/record/6505230#.Yz2FtdJByEA doi: 10.5281/zenodo.6505230

W. Cliver, E., & Cliver, E. W. (1994, 12). Solar activity and geomagnetic storms: The first 40 years. *EOS Transactions*, *75*(49), 569–575. Retrieved from https://onlinelibrary.wiley.com/doi/full/10.1029/94EO02041 doi: 10.1029/94EO02041

Weigel, R. S., Klimas, A. J., & Vassiliadis, D. (2003). Solar wind coupling to and predictability of ground magnetic fields and their time derivatives. *Journal of*

Geophysical Research: Space Physics, *108*(A7). doi: 10.1029/2002JA009627

Weygand, J. M., Amm, O., Angelopoulos, V., Milan, S. E., Grocott, A., Gleisner, H., & Stolle, C. (2012, 5). Comparison between SuperDARN flow vectors and equivalent ionospheric currents from ground magnetometer arrays. *Journal of Geophysical Research: Space Physics*, *117*(5), 5325. Retrieved from https://onlinelibrary.wiley.com/doi/full/10.1029/2011JA017407 doi: 10.1029/2011JA017407

Weygand, J. M., Amm, O., Viljanen, A., Angelopoulos, V., Murr, D., Engebretson, M. J., ... Mann, I. (2011, 3). Application and validation of the spherical elementary currents systems technique for deriving ionospheric equivalent currents with the North American and Greenland ground magnetometer arrays. *Journal of Geophysical Research: Space Physics*, *116*(3). Retrieved from https://onlinelibrary.wiley.com/doi/full/10.1029/2010JA016177 doi: 10.1029/2010JA016177

Weygand, J. M., Engebretson, M. J., Pilipenko, V. A., Steinmetz, E. S., Moldwin, M. B., Connors, M. G., ... Gjerloev, J. (2021, 11). SECS Analysis of Nighttime Magnetic Perturbation Events Observed in Arctic Canada. *Journal of Geophysical Research: Space Physics*, *126*(11), e2021JA029839. Retrieved from https://onlinelibrary.wiley.com/doi/full/10.1029/2021JA029839 doi: 10.1029/2021JA029839

Weygand, J. M., McPherron, R. L., Frey, H. U., Amm, O., Kauristie, K., Viljanen, A., & Koistinen, A. (2008, 4). Relation of substorm onset to Harang discontinuity. *Journal of Geophysical Research: Space Physics*, *113*(4). doi: 10.1029/2007JA012537

Weygand, J. M., & Wing, S. (2016, 6). Comparison of DMSP and SECS region-1 and region-2 ionospheric current boundary. *Journal of Atmospheric and Solar-Terrestrial Physics*, *143-144*, 8–13. doi: 10.1016/j.jastp.2016.03.002

Yee, J. H., Gjerloev, J., & Wu, D. (2021, 1). Remote Sensing of Magnetic Fields Induced by Electrojets From Space: Measurement Techniques and Sensor Design. In *Space physics and aeronomy, upper atmosphere dynamics and energetics* (pp. 451–468). wiley. doi: 10.1002/9781119815631.ch21

Zmuda, A. J., Martin, J. H., & Heuring, F. T. (1966, 11). Transverse magnetic disturbances at 1100 kilometers in the auroral region. *Journal of Geophysical Research*, *71*(21), 5033–5045. Retrieved from https://onlinelibrary.wiley.com/doi/full/10.1029/JZ071i021p05033 doi: 10.1029/jz071i021p05033